Uncertainties in Atmospheric River Life Cycles by Detection Algorithms: Climatology and Variability

Yang Zhou[1*], Travis A. O'Brien[2,1], Paul A. Ullrich[3,1], William D. Collins[1,4], Christina M. Patricola[5,1], and Alan M. Rhoades[1]

[1]Climate and Ecosystem Sciences Division, Lawrence Berkeley National Laboratory

[2]Department of Earth and Atmospheric Sciences, Indiana University, Bloomington

[3]Department of Land, Air, and Water Resources, University of California, Davis

[4]Department of Earth and Planetary Science, University of California, Berkeley, Berkeley

[5]Department of Geological and Atmospheric Sciences, Iowa State University

*Corresponding author: Yang Zhou (yzhou2@lbl.gov)

Key Points

- Detection algorithms introduce uncertainties in AR lifecycle characteristics such as event number, lifetime, intensity, and frequency.
- Agreement in landfalling AR activity among detection algorithms increases with stronger ARs.
- Uncertainties may be smoothed out when investigating AR activity at a time scale longer than ARs (such as intraseasonal and interannual).

Abstract

Atmospheric rivers (ARs) are long and narrow filaments of vapor transport responsible for most poleward moisture transport outside of the tropics. Many AR detection algorithms have been developed to automatically identify ARs in climate data. The diversity of these algorithms has introduced appreciable uncertainties in quantitative measures of AR properties and thereby impedes the construction of a unified and internally consistent climatology of ARs. This paper compares eight global AR detection algorithms from the perspective of AR life cycles following the propagation of ARs from origin to termination in the MERRA2 reanalysis over the period 1980-2017. Uncertainties related to lifecycle characteristics, including number, lifetime, intensity, and frequency distribution are discussed. Notably, the number of AR events per year in the Northern Hemisphere can vary by a factor of 5 with different algorithms. Although all algorithms show that the maximum origin (termination) frequency locates over the northwestern (northeastern) Pacific, significant disagreements occur in regional distribution. Spreads are large in AR lifetime and intensity. The number of landfalling AR events produced by the algorithms can vary from 16 to 78 events per cool season, i.e. by almost a factor of five, although the agreement improves for stronger ARs. By examining the AR's connection with the Madden-Julian Oscillation and El Niño Southern Oscillation, we find that the overall responses of ARs (such as changes in AR frequency, origin, and landfalling activity) to low-frequency climate variabilities are consistent among algorithms.

Plain Language Summary

Atmospheric rivers (ARs) are strong moisture transport in the atmosphere that is one of the dominant processes conveying water vapor from the tropics to high latitudes. ARs are also important water sources to coastal regions like the west coast of North America. Many studies have developed their own detection algorithms to study ARs. However, conclusions from these studies may differ because of different algorithm designs. Here we select an ensemble of eight detection algorithms and analyze the disagreement in AR characteristics across the ensemble including AR size, number, lifetime, intensity, and landfalling activity applied to a single dataset describing meteorological conditions in the recent past. Results suggest that basic AR characteristics vary significantly depending on the detection algorithm. Meanwhile, the large spread may be smoothed out when examining AR behavior in the intraseasonal and interannual time scale.

1. Introduction

Atmospheric rivers (ARs) are meteorological phenomena with a long and narrow filamentary structure of poleward moisture transport outside of the tropics. ARs are essential to the global hydrological cycle and are often linked to weather and climate extremes (Newell et al., 1992; Zhu & Newell, 1994). Due to their crucial role in water resources (Dettinger, 2013; Dettinger et al., 2011; Gorodetskaya et al., 2014) and their hydrological impacts of heavy precipitation and flooding (Lavers et al., 2011; Lavers et al., 2014; Neiman et al., 2013; Neiman et al., 2008; Ralph et al., 2006; Waliser & Guan, 2017), numerous studies have extensively investigated different aspects of ARs in the past two decades, including landfalling activity (Hu et al., 2017; Rutz et al., 2014), connections with low-frequency modes of climate variability (Gershunov et al., 2017; Guan & Waliser, 2015; Kim et al., 2017; Mundhenk et al., 2016; Payne & Magnusdottir, 2014), subseasonal-to-seasonal prediction (DeFlorio, Waliser, Guan, Lavers, et al., 2018; DeFlorio, Waliser, Guan, Ralph, et al., 2018; Lavers et al., 2014; Zhou & Kim, 2017), and future projections (Lavers et al., 2013; Payne & Magnusdottir, 2015; Radic et al., 2015; Shields & Kiehl, 2016b).

The American Meteorological Society (AMS) Glossary of Meteorology qualitatively defines an AR as "a long, narrow, and transient corridor of strong horizontal water vapor transport that is typically associated with a low-level jet stream ahead of the cold front of an extratropical cyclone", with no extant quantitative definition. Therefore, a great diversity of AR detection algorithms has emerged from research groups targeting different scientific questions. For example, in order to measure the impacts of AR's in-land penetration over North America, Rutz et al. (2014) defines an AR as regions where the magnitude of vertically-integrated moisture flux (IVT) exceeds 250 kg m^{-1} s^{-1} with lengths longer than 2000 km. Likewise, to understand global AR activity, Guan and Waliser (2015) defines an AR by applying a relative threshold on IVT (exceeding 85th

83 percentile) that varies spatially with other criteria on geometric shapes. However, the variety of
84 AR detection algorithms introduces uncertainties in AR measures and understanding of AR
85 activity. For example, Huning et al. (2017) show a 20% difference in ARs contribution to seasonal
86 cumulative snowfall over the Sierra Nevada when using an IVT-based versus integrated water
87 vapor (IWV)-based definition. To quantify and understand uncertainties that arise from different
88 AR detection algorithms, the Atmospheric River Tracking Method Intercomparison Project
89 (ARTMIP) was formed as an ad hoc, international collaboration (Shields et al., 2018). ARTMIP
90 includes over 30 (and growing) AR detection algorithms and is dedicated to providing guidance
91 on the most suitable algorithms for particular scientific applications. Ralph et al. (2018)
92 investigates ARs that made landfall in northern California using outputs from 10 AR detection
93 algorithms and concludes that the number of ARs can vary by a factor of two across this
94 representative set of algorithms. By examining the role of ARs in the western US watershed, Chen
95 et al. (2019) compares six detection algorithms and shows that the major difference from detection
96 algorithms is the precipitation amount, while the temperature changes in AR events are consistent
97 among algorithms. The ranges in AR climatological properties, including landfalling frequency
98 and duration, as well as seasonality, arising from the differences among ARs identified using 19
99 detection algorithms have been discussed in detail in Rutz et al. (2019).

100 These studies mainly focus on uncertainties in landfalling AR activity and related
101 hydrological impacts. Uncertainties in measures of AR origination and evolution over the ocean,
102 including frequency and propagation before landfall, have not been well-documented. Thus, in the
103 framework of ARTMIP, the goal of the present study is to understand uncertainties in ARs
104 stemming from detection algorithms within the context of AR life cycles. The life cycle of an AR
105 event records the complete propagation of AR-associated moisture transport from its origin to

termination. To track ARs spatiotemporally, an object-based automated AR tracking algorithm has been developed in Zhou et al. (2018) that can assemble the AR life cycles from the single time-level masks produces by different detection algorithms. With this tool in hand, we will address two questions: (1) To what degree are AR lifecycle characteristics (number, lifetime, intensity, and distributions of AR origin and termination) sensitive to the choice of AR detection algorithms? (2) Are the correlations between AR life cycles and various modes of climate variability (such as the Madden-Julian Oscillation (MJO) and El Niño Southern Oscillation (ENSO)) robust to the choice of detection algorithms? This study will be the first to apply a common tracking method across various AR detection algorithms and examine the associated uncertainties. It also provides a benchmark for AR life cycle sensitivities across detection algorithms. Further, this study has implications for improving prediction of AR activity by providing the degree of agreements among detection algorithms based on AR intensities and for reducing uncertainties in AR changes in the future climate by accessing the potentially well-suited algorithms in the context of projected AR life cycles.

In section 2, the AR detection algorithms selected from ARTMIP and the Zhou et al. (2018) AR life cycle tracking algorithm are introduced. Uncertainties in lifecycle characteristics are discussed in section 3. In sections 4 and 5 we investigate the sensitivity of AR connections with the MJO and ENSO respectively. Summary and discussion are provided in section 6.

2. Data and methods

2.1 Tracking AR life cycles from different detection algorithms

To investigate the uncertainty in AR life cycle stemming from detection algorithms, we use 15 of the global AR detection algorithms from the ARTMIP Tier 1 collection (Table 1) that

129 were available at the time of analysis. A more detailed description of participating ARTMIP Tier
130 1 algorithms and AR catalogues are provided in Shields et al. (2018). In ARTMIP Tier1, all
131 participants apply their algorithms to the 3-hourly 0.5-degree latitude by 0.625-degree longitude
132 Modern Era Retrospective analysis for Research and Applications, version 2 (MERRA2)
133 reanalysis from 1980-2017 (Gelaro et al., 2017). Note that some algorithms can be tuned for
134 particular scientific applications (such as Tempest), the included algorithms in this study are in
135 their default settings. As shown in Table 1, each algorithm has different thresholds on IVT or IWV
136 to detect ARs. There are two major kinds of thresholds: absolute thresholds specified by spatially
137 and temporally invariant values (e.g. AR-CONNECT and Rutz), and relative thresholds specified
138 by fixed percentiles of spatiotemporal varying IVT or IWV (e.g. Guan_Waliser and Lora_global).
139 Additional thresholds frequently employed by detection algorithms include geometric constraints
140 and machine learning techniques (e.g. TECA_bard_v1). We further largely focus our analysis on
141 the Northern Hemisphere.

142 We adopt the automated tracking algorithm developed by Zhou and Kim (2019); Zhou et
143 al. (2018) to identify the life cycle of AR events. The term "detection" and "tracking" are
144 sometimes used interchangeably by previous literature to describe AR identification. In this study,
145 we use "detection" for recognition of instantaneous AR conditions (i.e. AR objects, explained later)
146 and "tracking" for spatiotemporally tracing the life cycle of AR events. Therefore, we refer to the
147 selected ARTMIP algorithms as AR "detection" algorithms and the Zhou et al. (2018) algorithm
148 as the "tracking" algorithm. We define an AR object as an enclosed two-dimensional (latitude and
149 longitude) instantaneous area that meets the criteria of AR conditions. The life cycle of an AR
150 event is tracked by connecting the spatiotemporal overlapping AR objects (more details in section
151 3) from origin to termination.

152 2.2 Climate variability indices

153 We investigate the robustness of the relationships between ARs and low-frequency climate
154 variabilities with a focus on the MJO and ENSO. The Real-time Multivariate MJO index (RMM,
155 (Wheeler & Hendon, 2004)) is obtained to describe the MJO phase and amplitude. The MJO is
156 distinguished into eight phases depending on the location of enhanced convection using two RMM
157 components (Supplemental Figure S1). We define an MJO day when the RMM amplitude
158 ($\sqrt{\mathrm{RMM1}^2 + \mathrm{RMM2}^2}$) exceeds 1.0. We use daily interpolated 20-100-day-filtered outgoing
159 longwave radiation (OLR) (Liebmann & Smith, 1996) to indicate the location of MJO convection.

160 We use the ENSO Longitude Index (ELI, Williams and Patricola (2018)) to identify El
161 Niño and La Niña events. The ELI index is an SST-based metric that captures the average
162 longitude of Pacific tropical deep convection. We used ELI because it is able to characterize the
163 diversity of ENSO events in a single index (Williams & Patricola, 2018) and because it better
164 describes seasonal variations in western U.S. winter precipitation compared with other ENSO
165 indices (Patricola et al., 2020). For each month, the ELI index is calculated by first averaging the
166 sea surface temperature between 5°S-5°N. Next, a binary mask is created where equatorial
167 gridpoints with meridionally-averaged-SST exceeding the convection threshold (tropics-wide
168 averaged SST) are assigned a value of 1 and otherwise 0. Finally, the ELI index is the average of
169 longitudes of all the equatorial gridpoints with masks equaling 1. The ELI index is constructed
170 using monthly 2-degree Extended Reconstructed SST v5 (Huang et al., 2017) from December to
171 February from 1980-2016. The ENSO event is categorized by the absolute value of the ELI index.
172 We select the El Niño and La Niña years following the years of moderate and strong ENSO events
173 in Patricola et al. (2020) (in their Table 1). The same analysis is conducted with Niño 3.4 index
174 and SOI index and the results are consistent with the ELI index (not shown).

Acronyms	Reference	Type	Detection thresholds	Region
∗AR-CONNECT	Shearer et al. (2020)	Track	IVT = 300 kg m^{-1} s^{-1}, time-stitching for minimum 24 hours	Global
CONNECT500	Sellars et al. (2015); Sellars et al. (2013)	Track	IVT = 500 kg m^{-1} s^{-1}	Global
CONNECT700			IVT = 700 kg m^{-1} s^{-1}	
∗TECA_bard_v1	O'Brien et al. (2020)	Condition	Relative threshold (based on spatial percentile for each timestep). An inverted Gaussian filter is applied at the equator to damp out the ITCZ	Global
Cascade_ivt	Experimental	Condition	Convolutional neural network to replicate ARTMIP mean; Threshold free; use IVT as input	Global
Cascade_iwv			Same as above, but use IWV as input	Global
∗Guan_Waliser	Guan and Waliser (2015)	Condition	85th percentile IVT; Absolute minimum requirement designed for polar locations: 100 kg m^{-1} s^{-1} IVT	Global
∗Mundhenk_v3	Mundhenk et al. (2016)	Condition	IVT percentiles and/or anomalies both temporal and spatial	Global
Rutz	Rutz et al. (2014)	Condition	IVT (surface to 100mb) = 250 kg m^{-1} s^{-1}	Global
Sail_v1	Project: Atmospheric rivers identification, tracking and climatology assessment	Condition	80th percentile IVT; length-width ratio exceeds 5	Global
∗Lora_global	Lora et al. (2017)	Condition	Length >= 2000km; IVT 100kg$m^{-1}s^{-1}$ above climatological area means for the North Pacific	Global
∗Lora_v2			Length >= 2000km; Relative to 30-day running mean of background IWV	Global
Tempest_ivt250	Rhoades et al. (2020); McClenny et al. (2020)	Track	∇^2 IVT <= -4e4 kg m^{-1} s^{-1} rad^{-2}, IVT >=250 kg m^{-1} s^{-1}	Global, latitude ≥15°
∗Tempest_ivt500			∇^2 IVT <= -4e4 kg m^{-1} s^{-1} rad^{-2}, IVT >=500 kg m^{-1} s^{-1}	
∗Tempest_ivt700			∇^2 IVT <= -4e4 kg m^{-1} s^{-1} rad^{-2}, IVT >=700 kg m^{-1} s^{-1}	

Table 1. List of selected AR detection algorithms. More information is listed on http://www.cgd.ucar.edu/projects/artmip/algorithms.html. Algorithms marked with asterisk are adopted for extended analysis.

177

178 **3. Life-cycle characteristics**

179 Figure 1 shows the distributions of number, size, and overlapping ratio of AR objects
180 identified by 15 detection algorithms using global 3-hourly AR objects from the year 2016 (total
181 of 2928 time steps). We arbitrarily select the year 2016 to examine the characteristics of AR objects.
182 The average number of objects per time step varies from 6 to 42 (Figure 1a), where the lowest
183 number is from TECA_bard_v1 which includes a set of "plausible" AR detectors and the highest
184 number is from CONNECT500 which captures some tropical disturbances that may not be
185 associated with ARs or are entrained by ARs over their life cycle (e.g., tropical cyclones) (not
186 shown). About 10 algorithms detect 10-20 global AR objects at any given time step, which is
187 consistent with the number from a manual analysis by Newell et al. (1992) and the number range
188 of expert-identified global AR objects (O'Brien et al., 2020).

189 The probability distributions of object size and overlapping ratio vary among algorithms
190 (Figure 1b-c). The object size is represented by the number of gridpoints (0.5°×0.625°) within an
191 object. The overlapping ratio is a key parameter in the tracking algorithm, which is calculated as
192 the ratio of overlapping area with the object at previous time step *t-1* to the total area of object at *t*
193 (Zhou et al., 2018). A zero overlapping ratio of an object indicates the origin of an AR event.
194 Figures 1b-c suggest two types of distribution curves. The first type demonstrates a higher
195 percentage of smaller objects (less than 800 gridpoints) with a wider spread in overlapping ratio,
196 which may be due to identification of non-AR tropical disturbances that are usually smaller in size
197 (such as CONNECT500 and CONNECT700); or recognition of an IVT core that is smaller in size
198 (such as the Tempest family). The Cascade_iwv and Cascade_ivt algorithms determine an AR
199 object based on a machine learning algorithm trained on the consensus of all ARTMIP algorithms,

200 which makes them prone to identify primarily the IVT core, resulting in relatively smaller AR
201 objects. Algorithms showing the second type of distribution curve mostly capture the general long
202 and narrow shape of ARs (wider spread in object size) and present higher spatiotemporal
203 connectivity with more than 80% of overlapping ratio exceeding 0.7. However, some algorithms
204 detect objects with more than 5000 gridpoints (such as Rutz and Sail_v1), which may include the
205 Inter Tropical Convergence Zone (ITCZ). To exclude the impacts from ITCZ and tropical
206 disturbances, we narrow the selected algorithms down to eight algorithms for further analysis
207 (Table 1, marked with asterisks).

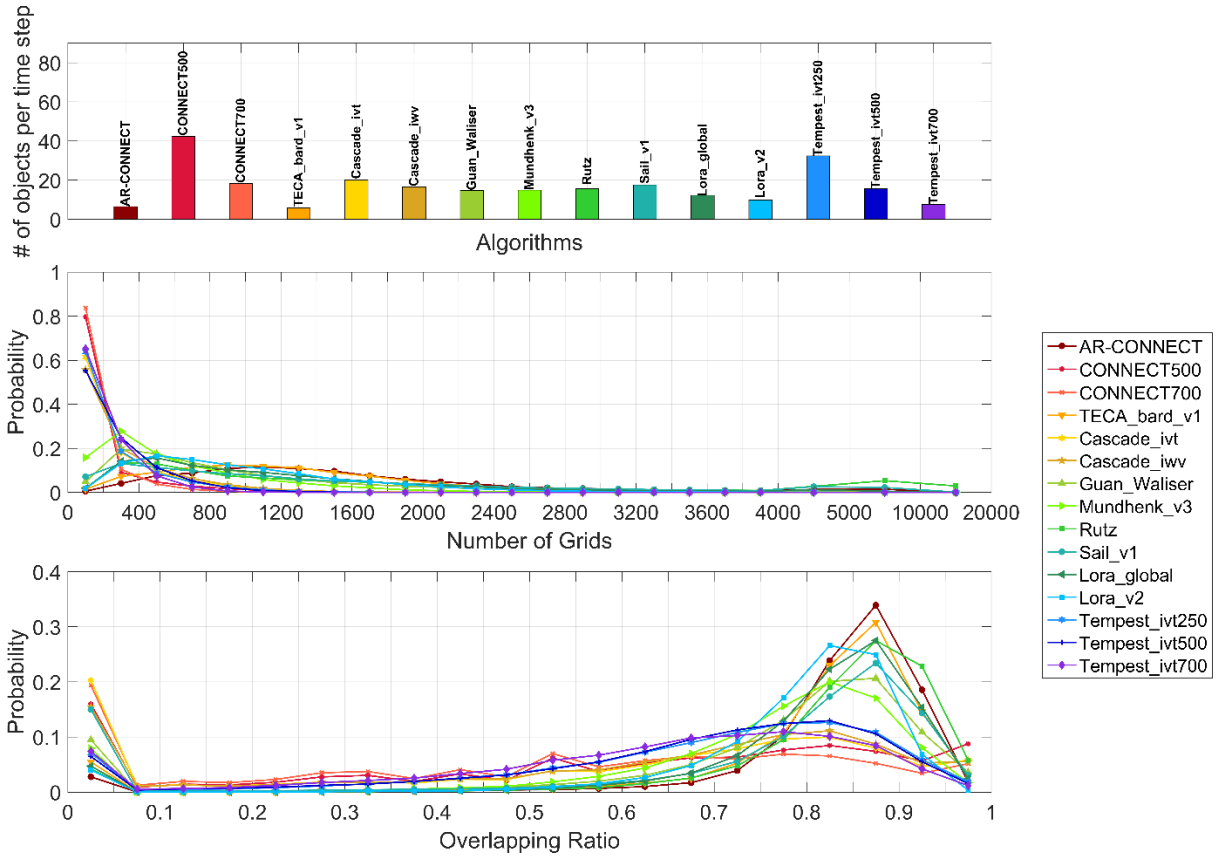

208

209 Figure 1. (a) Average number of global AR objects per time step. Probability distribution of (b)
210 object sizes and (c) overlapping ratio. Data: 3-hourly AR objects from the year 2016.

211

3.1 Climatology

Variations in the number and size of AR objects are reflected in the annual mean AR frequency (Figure 2). The AR frequency is calculated as, for each year, the gridpoint-accumulated number of AR objects normalized by the number of time steps (unit: percent of time steps). All algorithms show that in the Northern Hemisphere, high AR frequency appears over the ocean basin, where regions between 20°N-40°N are impacted by AR conditions about 10-30% of the time. AR frequency over the northwestern ocean basin is generally higher than that over the northeastern ocean basins. Due to higher IVT thresholds, the Tempest family naturally detects smaller AR objects and therefore shows a weaker amplitude of AR frequency (Figure 2g-h).

The origin (termination) object is defined as the first (last) object of an AR life cycle. The overall distribution of origin frequency is consistent among algorithms, with the maximum over the northwestern ocean between 20°N-40°N, which may be associated with more moisture by warmer sea surface temperature and more tropical cyclones. The disagreement between algorithms lies in the amplitude and regional distribution which are largely affected by the choice of threshold. The maximum termination frequency is concentrated over the eastern ocean and the west coast of North America and Europe. The termination frequency spreads more broadly in Guan_Waliser because more inland-penetrating AR activity being captured. Guan_Waliser also detects moisture transport activity over western Asia and the Arabian Peninsula, which may be linked to Somali Jet (Halpern & Woiceshyn, 1999). Overall, algorithms show agreement in the distributions of AR total, origin, and termination frequency. However, the uncertainties from algorithms may be large when it comes to regional studies, such as estimating the hydrological impacts from landfalling ARs (Rutz et al., 2019; Shields et al., 2018).

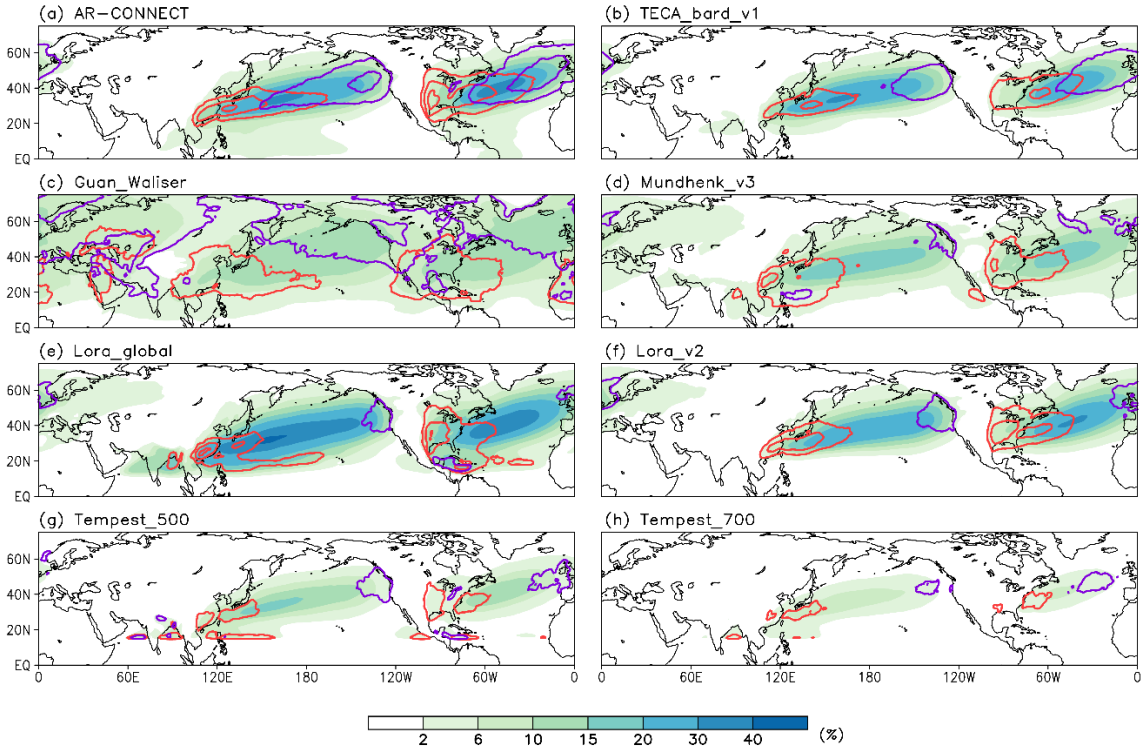

Figure 2. Annual mean total AR frequency (shading), origin (red contour), and termination frequencies (violet contour). Unit is percent of time steps. Note that shading intervals are not constant. Contour interval: (a-f) 0.2 percent of time steps and (g-h) 0.1 percent of time steps, zero lines are omitted.

The lifetime of an AR event represents how long an event lasts, which is calculated as the number of time intervals within the life cycle multiplied by the time interval (3 hours). All algorithms show that about 40-50% of North Pacific ARs (originated between 100°E-240°E) last less than 4 days (Figure 3a). About 40% of ARs detected by Guan_Waliser and Mundhenk_v3 last less than 2 days, which may be due to that one complete AR life cycle is identified as multiple life cycle pieces with shorter lifetimes because of some missing objects by these algorithms. This is reflected in Figure 3b which indicates the spatiotemporal connectivity by showing the mean AR lifetime and the annual number of North Pacific AR events. Algorithms closer to the lower right

corner suggest a relatively lower spatiotemporal connectivity – with a similar number range of AR objects per time step (Figure 1a), a greater number of AR events with shorter lifetime implies a higher chance of discontinuous life cycles. Algorithms closer to the upper left corner indicate higher spatiotemporal connectivity. These algorithms have more concentrated distributions of origin and termination frequency (Figure 2), suggesting more AR events originate over the northwestern Pacific, travel across the ocean, and terminate over the northeastern Pacific. The distribution of North Atlantic AR lifetimes is similar to that of the North Pacific ARs (Supplemental Figure S2). On average, North Atlantic ARs last one day shorter than the North Pacific ARs in most algorithms, which is mostly due to the shorter travel distance in the North Atlantic basin comparing with that in the North Pacific (Supplemental Figure S3). The travel distance of an AR event represents how long an AR event propagates during its life cycle, which shows a positive correlation with AR lifetime. The mean travel distance of North Pacific ARs can range from 5×10^3 km (Tempest_ivt700) to 15×10^3 km (Lora_v2). Generally, algorithms suggest that more than 80% of North Pacific and North Atlantic ARs travels within 25×10^3 km (Supplemental Figure S3).

The propagation speed is calculated by dividing the travel distance with AR lifetime, which shows how fast an IVT centroid travels during the life cycle (Figure 4a). The location of IVT centroid is determined by the mass-weighted averaged longitude and latitude within an object. Therefore, the propagation speed is impacted by the geometric consistency of AR objects in a life cycle – a sudden deformation of objects between two consecutive time steps can result in a spurious change in propagation speed. The Tempest family consistently detects the IVT core, which shows the most concentratedly distributed propagation speed with an average of about 59 km/hr. Other algorithms, with a broader range in object sizes (Figure 1b), present wider spread in propagation

271 speeds with averages ranging from 70-90 km/hr. Nearly identical distribution is shown with North
272 Atlantic ARs (Supplemental Figure S4a).

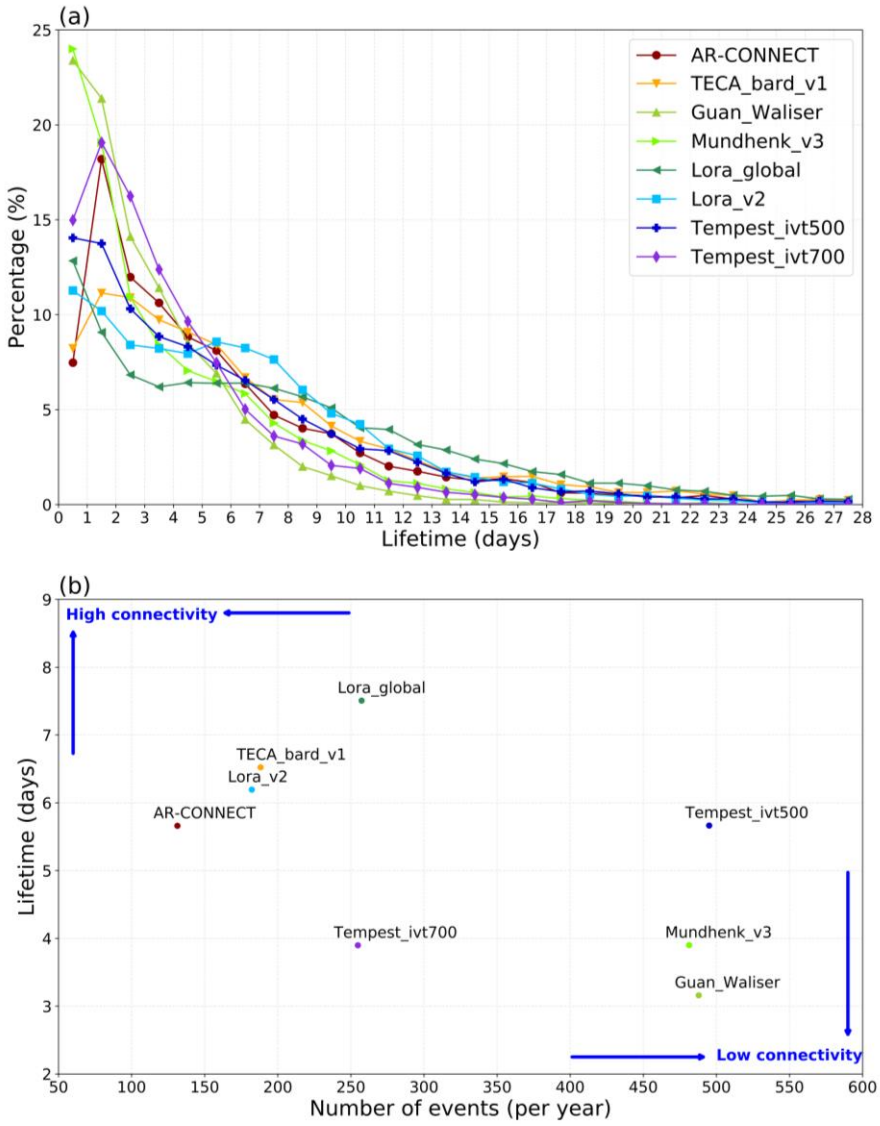

273

274 Figure 3. (a) Percentage distribution of North Pacific AR lifetime. (b) Scatter plot of the number
275 of North Pacific AR events per year and their mean lifetime.

276

277 The lifecycle intensity is calculated as the mean of domain averaged IVT magnitude (|IVT|)
278 within AR objects in the life cycle. Most algorithms detect lifecycle intensity in the range of 300-
279 800 kg m^{-1} s^{-1} (Figure 4b). Variations within this range can be due to subtle inconsistencies in the

binary masks of AR objects; wider (narrower) objects will tend to sweep up more points with lower (higher) IVT values. Guan_Waliser shows the largest spread in lifecycle intensity because their relative percentile threshold includes objects over land and the polar regions which possess weaker |IVT|. Spread is smaller in AR-CONNECT, Lora_global, and TECA_bard_v1. The lifecycle intensities of Tempest_ivt500 and Tempest_ivt700 are much stronger than other algorithms. The lifecycle intensity of North Atlantic ARs shows a similar distribution as the North Pacific ARs but with a smaller spread in most algorithms (Supplemental Figure S4b).

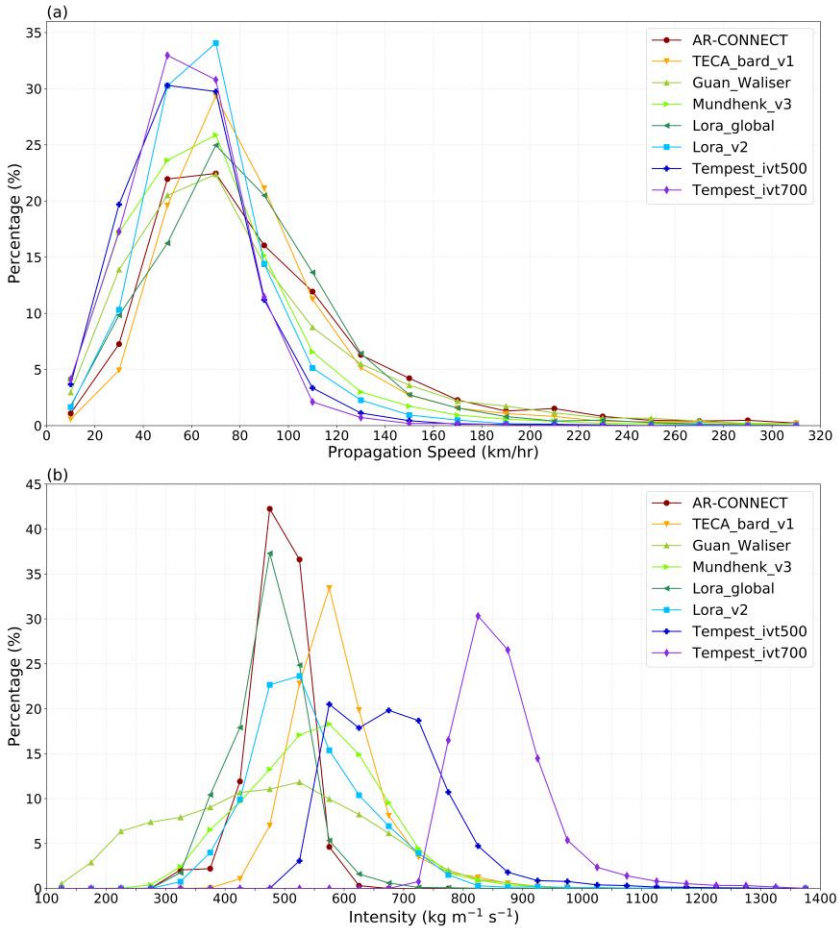

Figure 4. Distribution of (a) propagation speed (km/hour) and (b) lifecycle intensity (kg m^{-1} s^{-1}) for North Pacific AR events.

By comparing the number, lifetime, travel distance, propagation speed, and lifecycle intensity of AR events, we find that detection algorithms can introduce uncertainties in understanding the life cycle of AR events. The spatiotemporal connectivity plays a crucial role in determining the number and lifetime of AR events, and can further affect the distribution of AR origins and terminations, which can be problematic for examinations on AR's dynamical processes. The spread in lifecycle intensity may raise uncertainties in quantifying AR's contribution to the global hydrological cycle.

3.2 Landfalling ARs over North America

Although uncertainties in landfalling ARs have been extensively discussed within the ARTMIP literature, here we investigate the agreement of algorithms in the life cycle of landfalling ARs. We focus on the landfalling ARs over the west coast of North America (30°N-60°N) from November to March, which is the most active season of landfalling activity detected by the algorithms (not shown). We categorize the landfalling AR events into five categories following Ralph et al. (2019). The AR scaling criteria account for both landfalling duration and maximum landfall |IVT|. The AR category 1-5 is defined by maximum |IVT| of 250-1250 kg m^{-1} s^{-1} and by |IVT| exceeding 250 kg m^{-1} s^{-1} for 24-72 hours. Ralph et al. (2019) additionally recognizes landfalling ARs with |IVT| between 250-500 kg m^{-1} s^{-1} and duration less than 24 hours as weak ARs. From a water resources perspective, the weak ARs and Category 1-3 ARs (maximum |IVT| between 250-1000 kg m^{-1} s^{-1}) are generally beneficial and Category 4-5 ARs (maximum |IVT| between 1000-1250 kg m^{-1} s^{-1}) are mostly harmful primarily due to the risk of flooding and landslides. In Ralph et al. (2019), the determination of AR category is gridpoint-based, so the category for the same landfalling AR may vary depending on the location. Here, one AR event is categorized into one category with the maximum |IVT| over gridpoints and the landfall duration

of the entire event. Therefore, this study may overestimate the AR categories comparing to Ralph et al. (2019).

With the exception of the Tempest family, which misses the weaker categories due to more restrictive parameter selections, the number of landfalling AR events ranges from 37 to 78 events per season among algorithms (Figure 5a), with the highest number in Guan_Waliser, which captures the most in-land AR activity (Figure 2c). Interestingly, although there is a large discrepancy in landfalling event numbers, percentages in each AR category are similarly distributed among algorithms. Weak and Category 1-2 ARs take up about 20% of total landfalling events respectively for most algorithms. About 15-17% of landfalling ARs are Category 3 and the percentage drops to 12-14% for Category 4. About 4-7% of landfalling ARs are attributed to Category 5. No weak ARs (weak & Category 1 ARs) are identified with Tempest_ivt500 (Tempest_ivt700). Percentages of Category 4 and 5 ARs are lower in Tempest algorithms, which may be due to a shortened landfall duration caused by relatively higher IVT thresholds than other algorithms.

How does the agreement in algorithms change in different AR categories? For each AR category and each algorithm, we create a time series with landfalling stamps: a day is marked as 1 if it is a landfalling day and 0 otherwise. Next, for each AR category, we add the time series of all algorithms to calculate the number of algorithms agreeing on the same landfalling days. For example, if the number equals 5, it means five algorithms detect a landfalling AR on that day. Note that the number of algorithms in agreement can change during the same landfalling AR event because the landfall duration may vary by algorithms. The percentage in Figure 5b is calculated as the number of algorithms in agreement divided by the total number of landfalling days in each category. The number of algorithms in agreement increases with AR category. 70% of landfalling

days by weak ARs are only detected by one algorithm, indicating that most algorithms are not detecting the same weak ARs. On the other hand, about 50% of landfalling days affected by Category 5 ARs are detected by at least three algorithms. Although the inclusion of the two Tempest algorithms may potentially underestimate the number percentage, the result suggests that the uncertainty among algorithms is much smaller with stronger ARs.

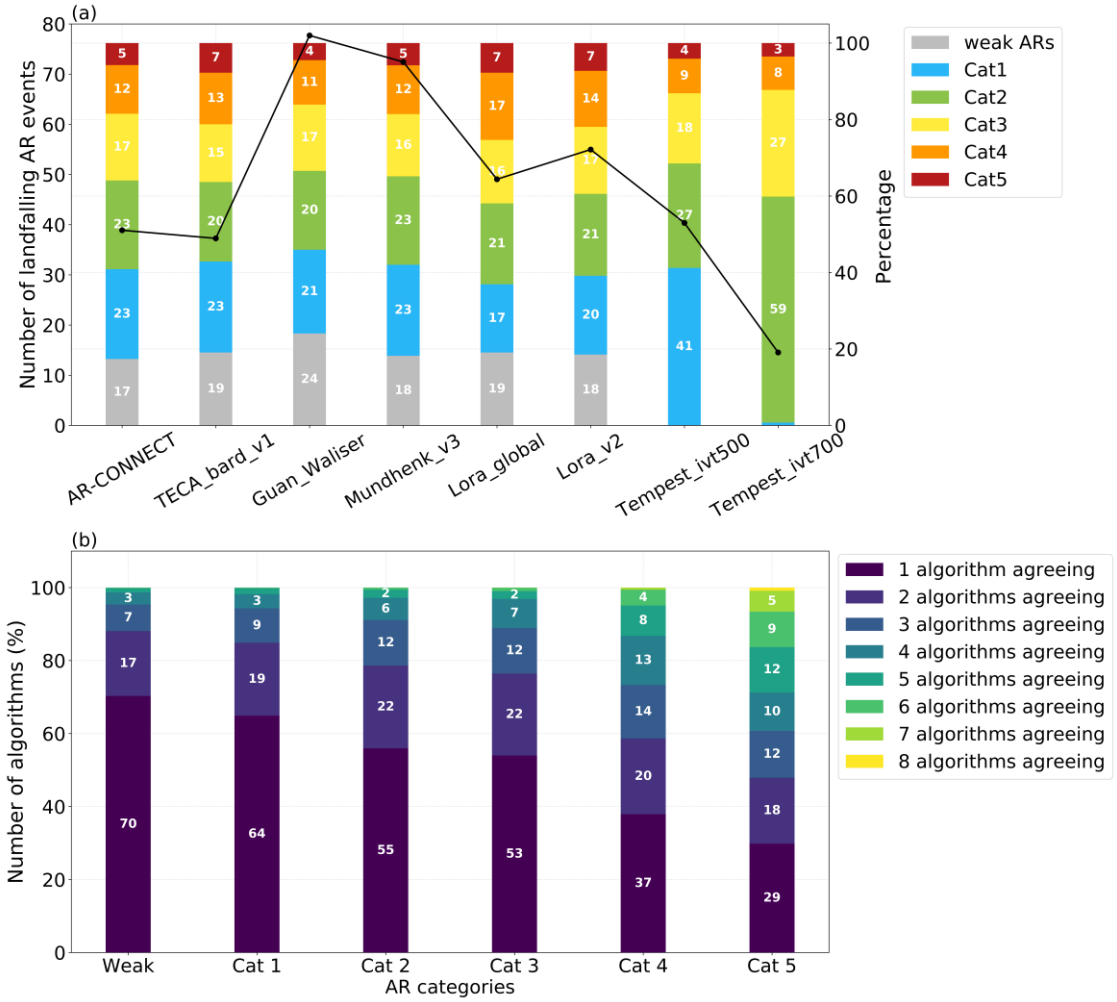

Figure 5. (a) (Line, left y-axis) Number of landfalling AR events per winter season over the west coast of North America. (Bar, right y-axis) Percentage of landfalling events in each AR category. (b) Percentage of the number of algorithms in agreement. Numbers in (a-b) annotate the percentage.

4. MJO-AR connections

Previous studies have discussed how ARs may be impacted by the MJO, including associated landfalling activity, AR-related hydrological impacts, and subseasonal AR prediction (Baggett et al., 2017; Guan et al., 2013; Guan & Waliser, 2015; Guan et al., 2012; Mundhenk et al., 2016; Mundhenk et al., 2018; Payne & Magnusdottir, 2014; Ralph et al., 2011). Here, we examine the linkage between ARs and the MJO from the lifecycle perspective to evaluate the robustness of such linkages. To investigate the MJO's influence on AR life cycles, we select AR events that *originate concurrently* with the MJO phases. In each MJO phase, the composite for each algorithm is calculated by subtracting the respective winter climatology (Supplemental Figure S5) and dividing by the number of MJO days in that phase. For a clear comparison, all composites are normalized to show the relative percentage changes.

Figure 6 shows the percentage changes in AR lifecycle frequency during MJO phase 2, when enhanced (suppressed) convection is located over the Indian Ocean (western Pacific). For each AR event, the lifecycle frequency is calculated as the summation of binary mask for each AR object within the event and therefore summarizes the overall area impacted by an AR life cycle. During MJO phase 2, a geopotential high anomaly persists over the North Pacific (Supplemental Figure 1b) and induces an anticyclonic flow with equatorward and westward flow over the northeastern Pacific and poleward and eastward flow over the northwestern Pacific (Stan et al., 2017). Algorithms overall present similar changes in lifecycle frequency during MJO phase 2, with about 10-30% decrease over the subtropical and northeastern Pacific, and approximately 30-50% increase near eastern Asia. Most algorithms suggest reduced AR activity over North America, where Guan_Waliser shows the strongest reduction, with a nearly 10-30% decrease of in-land lifecycle frequency between 30°N-60°N. Over the North Atlantic, an approximately 10% increase

of lifecycle frequency occurs between 25°N-60°N, which may be associated with the increased tropical cyclone activity during MJO phase 2 (Barnston et al., 2015; Maloney & Hartmann, 2000; Mo, 2000). The increased lifecycle frequency over the North Atlantic is stronger in Tempest_ivt500 and Tempest_ivt700, which implies that responses in North Atlantic ARs to the MJO may be stronger for ARs with greater intensity.

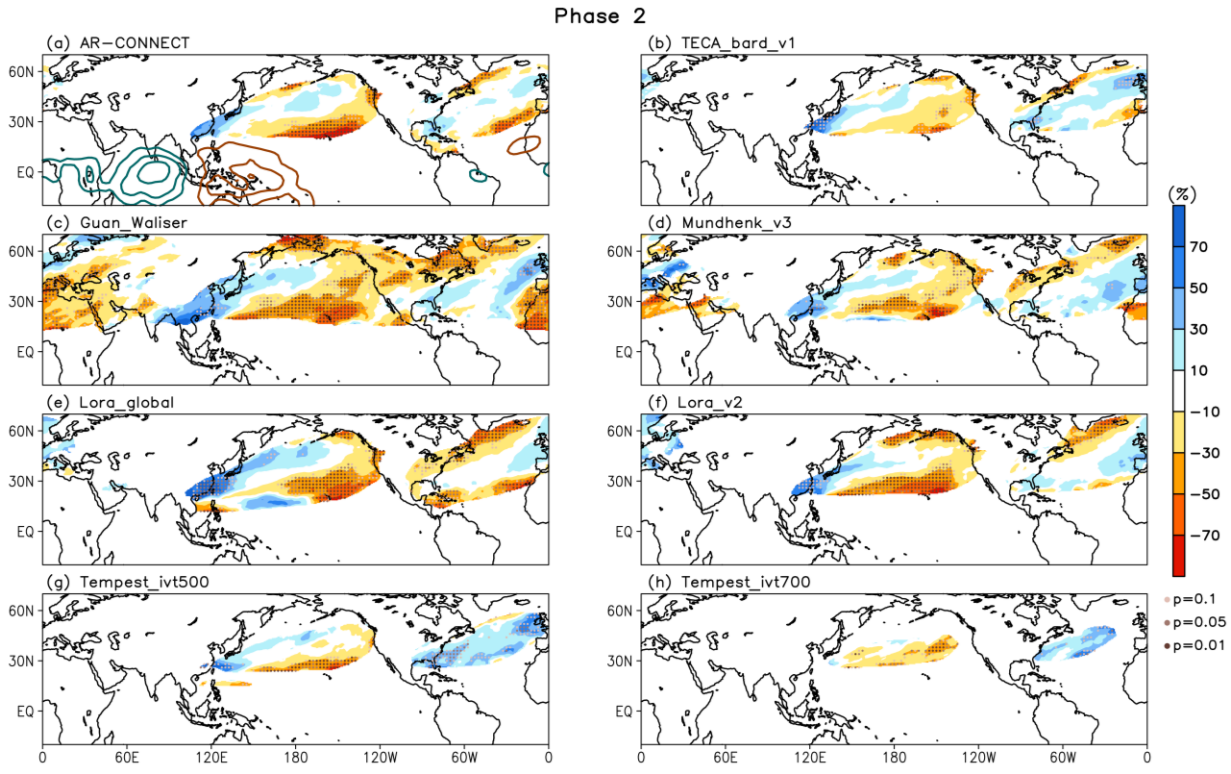

Figure 6. Shading: percentage changes in cool-season AR lifecycle frequency during MJO phase 2. Dots mark areas of different p-values. Contour in (a): 20-100-day-filtered OLR anomaly (blue/orange means negative/positive value, 5 W m^{-2} interval, zero line is omitted).

Algorithms show qualitatively similar changes in AR origin frequency over the North Pacific during the MJO phases 1-8 (Figure 7). The origin frequency is meridionally averaged between 20°N-40°N which is the latitudinal range of maximum origin frequency (Figure 2). All

algorithms capture the increased origin frequency between 100°E-120°E during phases 1-2 when the MJO convection is over the Indian Ocean, with an average increase of 35%, excluding the Tempest_ivt700 which shows an increase of 200%. The large increase in Tempest_ivt700 may be due to its weakest winter climatology among algorithms (Supplemental Figure S5h). The increased origin frequency extends eastward to 140° E as the MJO convection propagates eastward to the west lateral of the Maritime Continent during phase 3. The increased origin frequency may be related to increased moisture content coupled with enhanced tropical convection (Bretherton et al., 2004; Holloway & Neelin, 2009). Meanwhile, decreased origin frequency emerges near 140°E-160°E during phases 1-3. Changes in origin frequency over the northwestern Pacific are associated with a Gill type response to MJO forcing (Bao & Hartmann, 2014; Gill, 1980). Additionally, decreased origin frequency occurs near 140°W during phase 2, which is associated with the anomalous high over the northeastern Pacific (Supplemental Figure 1b). On average, the origin frequency over the northeastern Pacific (170°E-140°W) is decreased by 30%.

Roughly opposite changes in origin frequency emerge during MJO phase 5-6 when the enhanced convection is over the western Pacific (Figure 7e-g). Decreased origin frequency occurs over eastern Asia and the northwestern Pacific and increased origin frequency emerges between 140°E-160°E. The maximum increase in origin frequency is over the northeastern Pacific, which is impacted by the anomalous low anomaly during MJO phase 7 (Stan et al., 2017; Supplemental Figure S1g). This is consistent with previous studies suggesting that AR activity is likely to increase when enhanced tropical convection is over the western Pacific (phase 6-7) (Guan et al., 2012; Payne & Magnusdottir, 2014; Spry et al., 2014). Changes during phases 4 and 8 are relatively weaker and noisier comparing to other MJO phases. The same calculation is done with North Atlantic AR life cycles (Supplemental Figure S6). Similar changes among algorithms appear

406 during MJO phases 1-2 with increased origin frequency over the northeastern Atlantic which is
407 consistent with Figure 6. Overall, for both the North Pacific and North Atlantic, changes in AR
408 origin and lifecycle frequency by the MJO are qualitatively agreeable among detection algorithms,
409 although regional disagreement exists due to uncertainties in identifying the origin of AR events
410 and determining object sizes.

411 To evaluate the robustness of the MJO's impact on landfalling ARs, we calculate the
412 domain average of landfalling AR frequency along the west coast of North America. A mask with
413 10° longitudinal width is created following the coastline. Three domains are selected including
414 California, Oregon and Washington, and British Colombia. Figure 8 shows the lagged composites
415 of percentage changes in landfalling AR frequency over California by MJO phases. For example,
416 day 0 is when the MJO is in-phase and day 6 represents six days after day 0. The MJO's impact
417 on landfalling ARs is persistent during the MJO's lifecycle. AR activity over California is
418 significantly decreased (about 30-45%) from lag 12-24 days after phase 1 to lag 5-14 days after
419 phase 3 in all algorithms. From lag 13-18 days after phase 5 to lag 0-5 days after phase 7, an
420 approximate increase of 25-35% in AR frequency emerges. A similar pattern is shown in
421 Mundhenk et al. (2018). Responses in Tempest_ivt700 are particularly intense, with an
422 approximate 70% decrease during phases 1-3 and a nearly 80% increase during phases 5-7. This
423 could be because Tempest_ivt700 has a relatively weaker climatology because of the higher IVT
424 threshold (Supplemental Figure S5h); alternatively, stronger ARs may be more sensitive to the
425 MJO. Similar but shifted patterns appear in the lagged composites of Oregon and Washington as
426 well as British Colombia (Supplemental Figure S7-8).

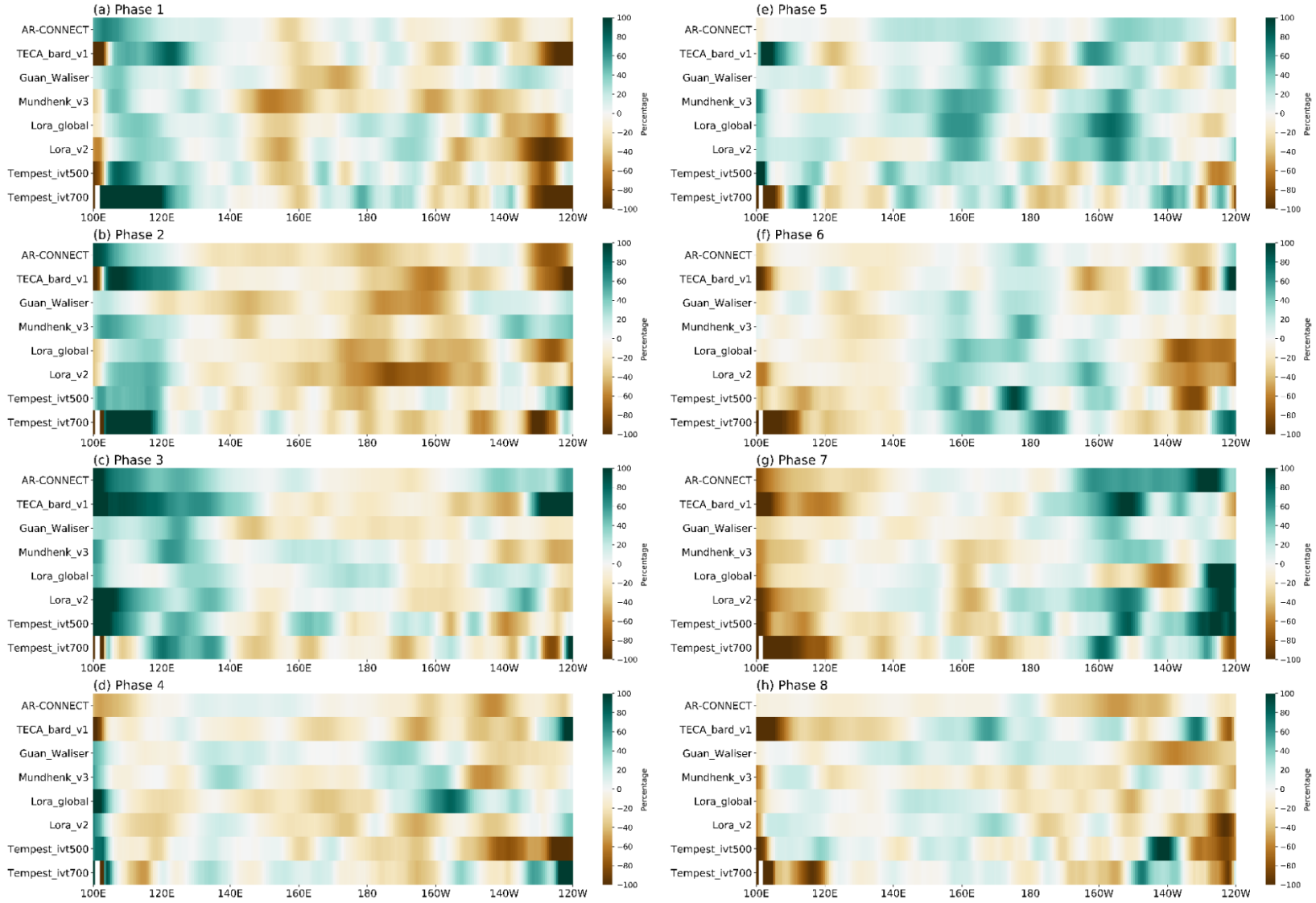

Figure 7. Percentage changes in North Pacific origin frequency during (a-h) MJO phase 1-8.

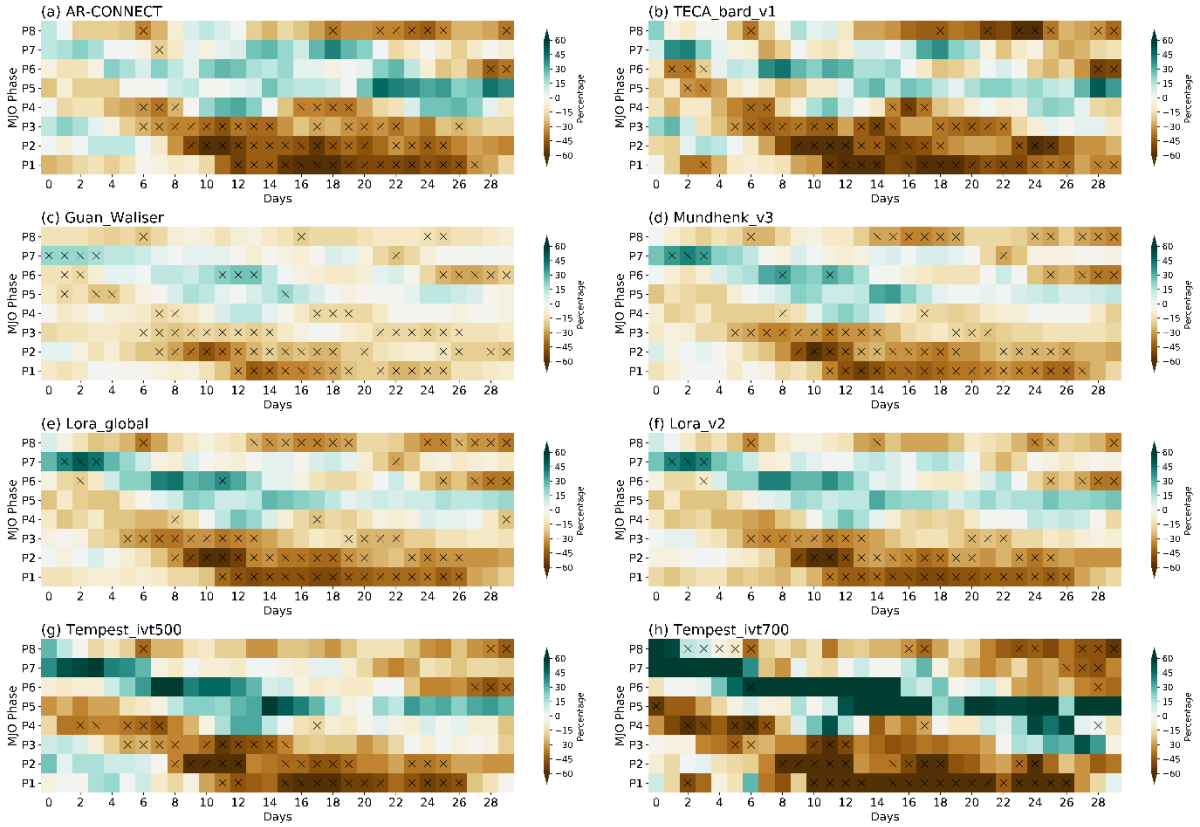

Figure 8. Percentage changes in landfalling AR frequency over California during MJO phase 1-8. The x-axis represents the days after an in-phase MJO. The dot marks the day that exceeds the 95% significant level of a one-sample t-test.

5. ENSO-AR connections

How ENSO modulates AR activity has been examined in several studies (e.g., Guan & Waliser, 2015; Kim et al., 2017; Mundhenk et al., 2016; Patricola et al., 2020; Payne & Magnusdottir, 2014; Ryoo et al., 2013), especially over the northeastern Pacific. During El Niño winters when the anomalously warm SST gathers over the tropical eastern Pacific (Figure 9a), a deepened Aleutian Low prevails over the northeastern Pacific, which is associated with the equatorward-shifted and eastward-extended subtropical jet (not shown). Previous studies have concluded that correspondingly, more zonal moisture transport occurs during El Niño winter,

442 which is represented by increased AR activity over the northeastern Pacific and the west coast of
443 U.S. around 30°N-45°N (e.g., Kim et al., 2017; McGuirk et al., 1987; Patricola et al., 2020).

444 Here, we calculate the changes in lifecycle frequency to evaluate the robustness of the
445 ENSO-AR connection. All algorithms show a zonal band of increased lifecycle frequency between
446 20°N-40°N with two maximum centers over the northeastern and northwestern Pacific. Changes
447 in AR activity over the northeastern Pacific are closely modulated by the deepened Aleutian Low
448 (Kim et al., 2017). All algorithms demonstrate a 10-30% increase of lifecycle frequency between
449 30°N-45°N which is associated with the northeastward IVT anomaly at the south branch of the
450 intensified Aleutian Low (e.g. Figure 2a in Kim et al. (2017)). The maximum decrease in lifecycle
451 frequency between 40°N-60°N is associated with the southwestward IVT anomaly at the north
452 branch of the anomalous low. Over the northwestern Pacific, the AR origin frequency is
453 significantly increased by at least 30% over eastern Asia. The decreased origin frequency near
454 20°N is linked to the decreased lifecycle frequency over the subtropical central Pacific.
455 Mechanisms associated with the changes in AR origin frequency over the northwestern Pacific
456 have not been discussed extensively by previous studies. Possible hypotheses include impacts from
457 the subtropical jet and geopotential height pattern (Patricola et al., 2020), or the joint impact from
458 the MJO and ENSO (Lau & Chan, 1988; Moon et al., 2011), which we will investigate in the future
459 study. Significant changes also appear over the North Atlantic: all algorithms show the increased
460 origin and lifecycle frequency along the U.S. east coast, which is likely associated with the
461 increased extratropical cyclone activity during El Niño (Chang et al., 2002; Eichler & Higgins,
462 2006; Hirsch et al., 2001).

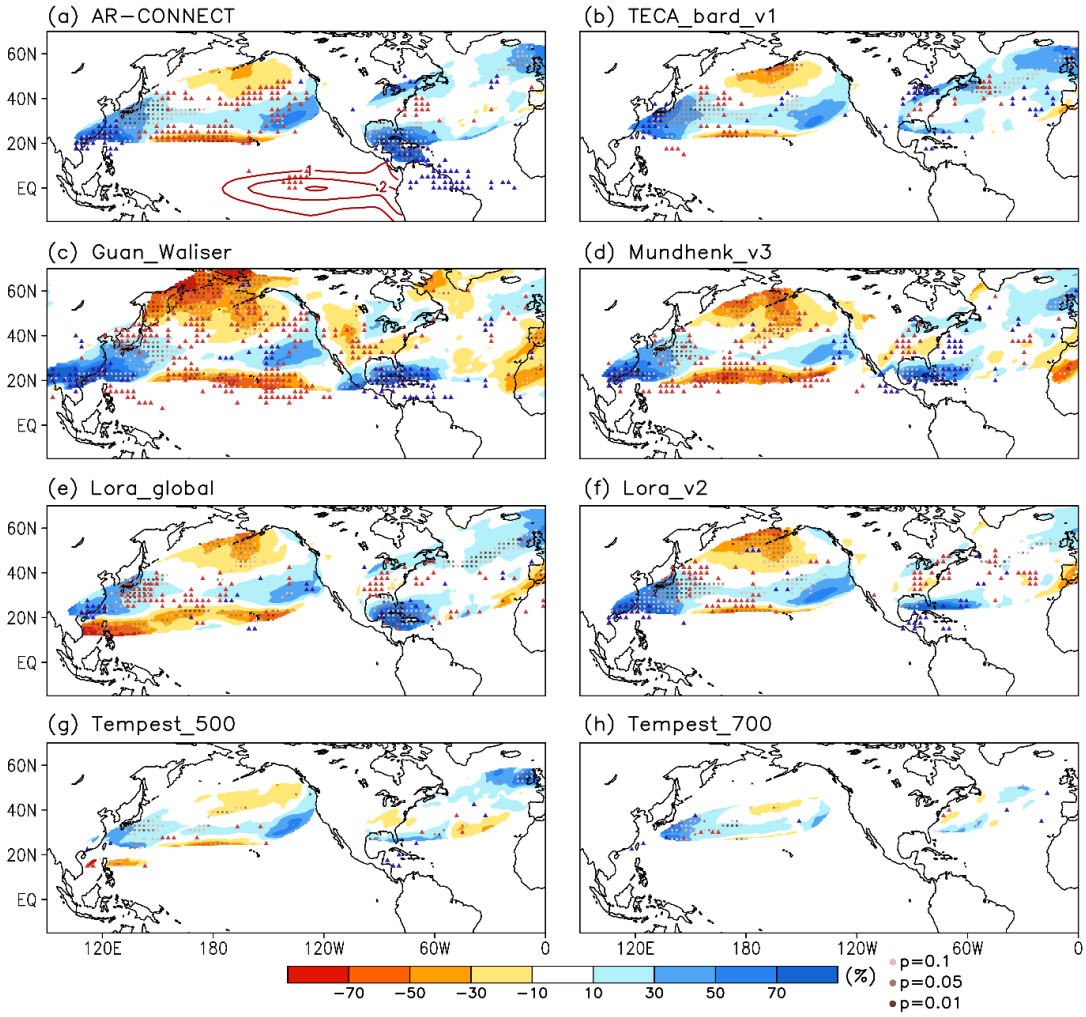

Figure 9. Shading: percentage changes in AR lifecycle frequency during El Niño years. Dots mark the areas of different p-values. Blue/red solid triangle markers indicate areas with increased/decreased origin frequency exceeding 30% and passing the 95% confidence level of a one-sample t-test. Contours in (a) indicate the SST anomaly during El Niño.

A nearly opposite pattern of changes in lifecycle frequency is shown during La Niña winters when cold SST anomaly concentrates in the central and eastern Pacific (Figure 10a). Changes in lifecycle frequency present consistent patterns over the northeastern Pacific in all algorithms. Decreased frequency, with a peak of 70%, appears near the U.S. west coast. Increased

lifecycle frequency occurs between 40°N-60°N over the central Pacific, which is associated with the northeastward IVT anomaly at the northwest branch of the anomalous high. Opposite responses in AR origins and lifecycle frequency emerge over the northwestern Pacific but in a weaker amplitude comparing to El Niño. The asymmetry between El Niño and La Niña is discussed in previous studies (e.g., An et al., 2005; An & Jin, 2004; Gershunov & Barnett, 1998; Hoerling et al., 1997). Interestingly, a regional increase in lifecycle frequency occurs over the western US coast near 30°N during La Niña in some algorithms (Figure 10c-f), which tends to be similar during El Niño. Also, a roughly 50% decrease in lifecycle frequency is shown over the North Atlantic between 20°N-40°N and extends eastward to the southern part of the west coast of Europe.

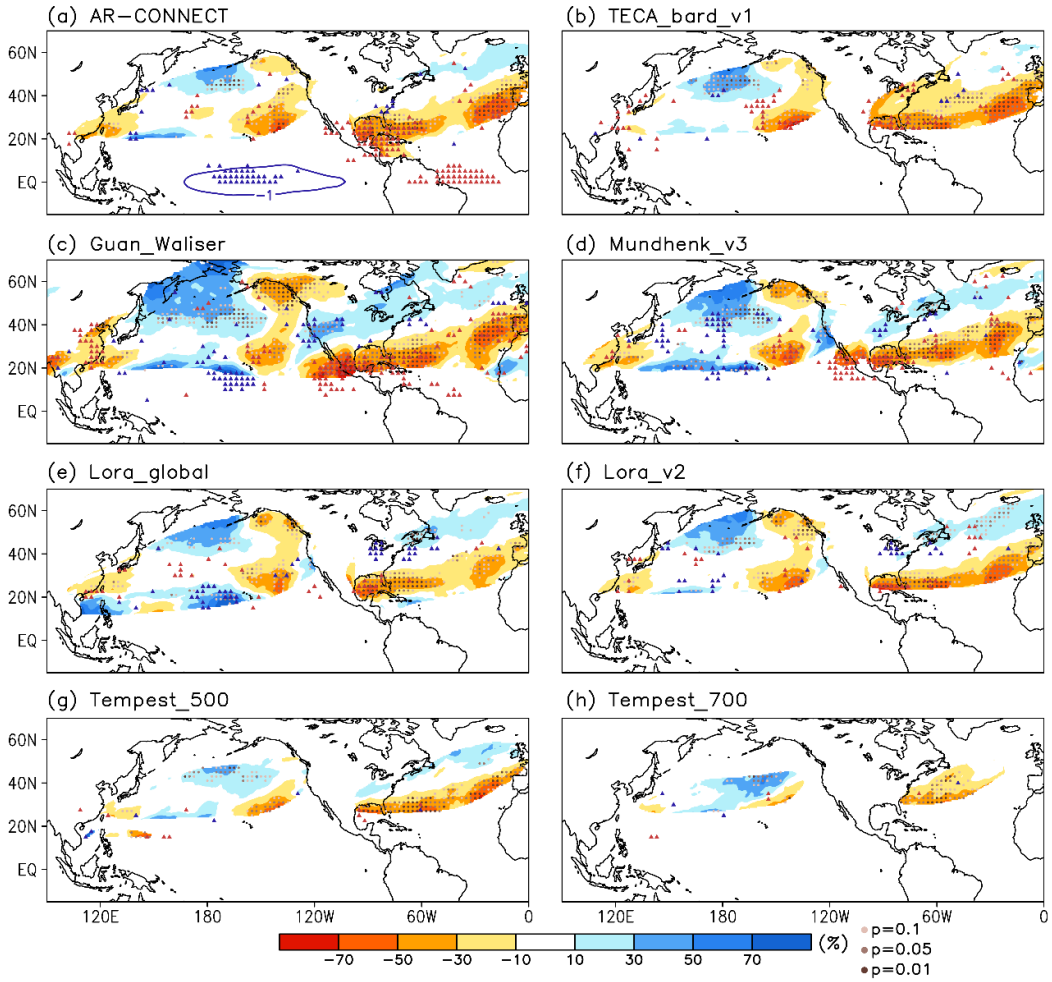

Figure 10. Same as Figure 9 but for La Niña years.

6. Summary and discussion

It has been a community effort to understand and quantify the uncertainties in AR research caused by detection algorithms. In this study, we specifically investigate the uncertainties of AR life cycles stemming from detection algorithms including their characteristics and connections to climate variabilities. Eight global algorithms are selected from the ARTMIP Tier 1 dataset. Results suggest that uncertainties in lifecycle characteristics (such as number of events, lifetime, travel distance, propagation speed, and intensity) can be large among algorithms. Such uncertainties are mainly caused by discrepancies in object sizes and spatiotemporal connectivity due to different algorithm design (e.g., choice of threshold and geometric constraint). Previous literature discussed the sensitivity of AR characteristics to detection methods concerning algorithm development (e.g., Guan & Waliser, 2015; Mundhenk et al., 2016; Rutz et al., 2014), our study extends this discussion to multiple algorithms with the perspective of AR life cycles.

Because of the significant hydrological impacts of ARs, the spread in landfalling AR activity over the west coast of North America by detection algorithms has been extensively discussed by previous ARTMIP publications (references in Section 1). We evaluate the spread in number of landfalling AR events and the agreement on landfalling AR category impact scaling among algorithms. The number of landfalling AR life cycles can vary from 15 events per winter to 78 events per winter by different algorithms. Results suggest that algorithms' agreement in AR landfalling days increases with higher AR categories although the lifecycle characteristics may vary. For example, Figure 11 shows the propagation tracks identified by different algorithms of a Category 5 AR that made landfall over California around February 7, 2015, which is in association with hourly precipitation amounts > 8 mm/hr (Cordeira et al., 2017). All eight algorithms detected

this landfalling AR. However, while most algorithms identify the origin of this AR event between 25°N, 170°E-160°W and show the northeastward propagation of moisture transport, two algorithms suggest different origin locations near 35°N, 150°W, which is likely due to merging of objects during propagation. The propagation tracks start to wobble when approaching to the coast because the shape and size of AR objects may change quickly as rapid depletion of IVT via precipitation upon landfall. Figure 11 indicates that when focusing on the physical processes such as mechanisms for AR origins and the path along which the AR propagates, the uncertainty introduced by detection algorithms may impede the understanding and interpretation of AR activity. For the same moisture transport event, the points of origin and termination vary by algorithms. This could be problematic when predicting the evolution of ARs or forecasting AR-related precipitations.

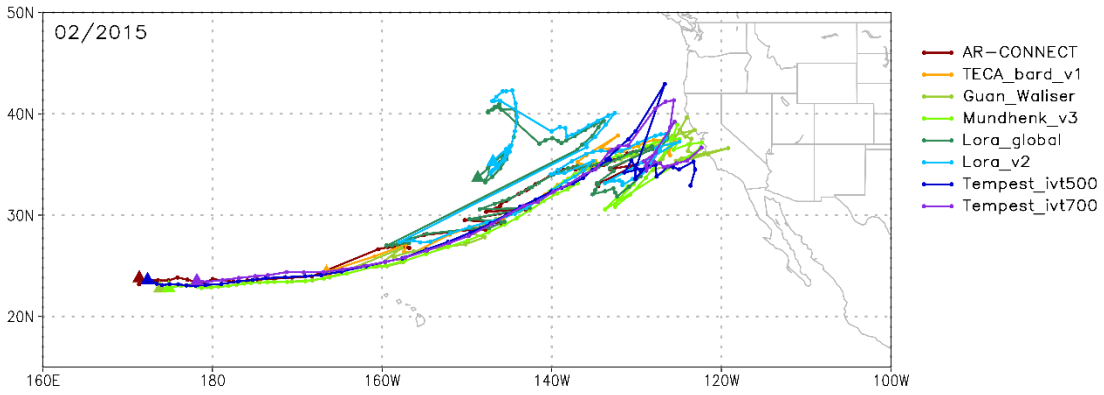

Figure 11. Example of propagation tracks of a landfalling AR event in early February 2015. Solid triangles mark the locations of AR origins detected by algorithms.

Additionally, the robustness of the MJO-AR and ENSO-AR connections across different algorithms is discussed. The overall AR responses to the MJO and ENSO are maintained despite differences in detection algorithms, indicating that the uncertainties in AR life cycles by detection algorithms may be smoothed out when investigating AR activity in a time scale longer than ARs

(such as connections with the MJO and ENSO). However, disagreements in regional distribution of origin and total frequency imply the challenges in quantifying AR's response to climate variabilities.

Although there is a lack of consensus for a quantitative definition of ARs, various studies have quantitatively defined ARs for analysis and modeling, which primarily leads to uncertainties in AR measures (Rutz et al., 2019; Shields et al., 2018) including the spread in AR life cycles discussed in this study. Such uncertainties could also cause variations in quantifying changes of future ARs such as object sizes, frequency, and other lifecycle characteristics (Espinoza et al., 2018; Radic et al., 2015; Shields & Kiehl, 2016a). A better understanding of the physical processes associated with different stages in AR life cycle (such as origin, propagation, landfall, and termination) is crucial to mitigate uncertainties in AR-related research. This study provides a useful tool to analyze the mechanisms associated with each stage of AR life cycles and to conduct uncertainty analysis with multiple algorithms. An effort like this could help to pave the way toward a quantitative theory of AR origins and terminations, which has great implications on improving AR predictions and advancing the understanding of future ARs.

Acknowledgments

This study was funded by the Director, Office of Science, Office of Biological and Environmental Research of the U.S. Department of Energy Regional and Global Climate Modeling Program (RGCM) "the Calibrated and Systematic Characterization, Attribution and Detection of Extremes (CASCADE)" Science Focus Area (award no. DE-AC02-05CH11231). Analysis was performed using the National Energy Research Scientific Computing Center (NERSC).

All ARTMIP data are available from the Climate Data Gateway, DOI:10.5065/D6R78D1M (ARTMIP Tier 1 Catalogues)

The OLR is provided by the NOAA/OAR/ESRL PSD, Boulder, Colorado, USA, from their Web site at https://psl.noaa.gov/data/gridded/data.interp_OLR.html.

The Extended Reconstructed SST v5 data is provided by the NOAA/OAR/ESRL PSL, Boulder, Colorado, USA, from their Web site at https://psl.noaa.gov/data/gridded/data.noaa.ersst.v5.html.

The Real-time Multivariate MJO index is obtained from the Bureau of Meteorology from Australian Government at http://www.bom.gov.au/climate/mjo/graphics/rmm.74toRealtime.txt.

560 **Reference**

561 An, S. I., Ham, Y. G., Kug, J. S., Jin, F. F., & Kang, I. S. (2005). El Niño–La Niña Asymmetry in
562 the Coupled Model Intercomparison Project Simulations*. *Journal of Climate, 18*(14),
563 2617-2627. doi:10.1175/jcli3433.1

564 An, S. I., & Jin, F. F. (2004). Nonlinearity and Asymmetry of ENSO. *Journal of Climate, 17*(12),
565 2399-2412. doi:10.1175/1520-0442(2004)017<2399:NAAOE>2.0.CO;2

566 Baggett, C. F., Barnes, E. A., Maloney, E. D., & Mundhenk, B. D. (2017). Advancing atmospheric
567 river forecasts into subseasonal-to-seasonal time scales. *Geophysical Research Letters,*
568 *44*(14), 7528-7536. doi:10.1002/2017gl074434

569 Bao, M., & Hartmann, D. L. (2014). The response to MJO-like forcing in a nonlinear shallow-
570 water model. *Geophysical Research Letters, 41*(4), 1322-1328. doi:10.1002/2013gl057683

571 Barnston, A. G., Vigaud, N., Long, L. N., Tippett, M. K., & Schemm, J. E. (2015). Atlantic
572 Tropical Cyclone Activity in Response to the MJO in NOAA's CFS Model. *Monthly*
573 *Weather Review, 143*(12), 4905-4927. doi:10.1175/mwr-d-15-0127.1

574 Bretherton, C. S., Peters, M. E., & Back, L. E. (2004). Relationships between water vapor path
575 and precipitation over the tropical oceans. *Journal of Climate, 17*(7), 1517-1528. doi:Doi
576 10.1175/1520-0442(2004)017<1517:Rbwvpa>2.0.Co;2

577 Chang, E. K. M., Lee, S. Y., & Swanson, K. L. (2002). Storm track dynamics. *Journal of Climate,*
578 *15*(16), 2163-2183. doi:Doi 10.1175/1520-0442(2002)015<02163:Std>2.0.Co;2

579 Chen, X. D., Leung, L. R., Wigmosta, M., & Richmond, M. (2019). Impact of Atmospheric Rivers
580 on Surface Hydrological Processes in Western U.S. Watersheds. *Journal of Geophysical*
581 *Research: Atmospheres, 124*(16), 8896-8916. doi:10.1029/2019jd030468

582 Cordeira, J. M., Ralph, F. M., Martin, A., Gaggini, N., Spackman, J. R., Neiman, P. J., . . . Pierce,
583 R. (2017). Forecasting Atmospheric Rivers during CalWater 2015. *Bulletin of the*
584 *American Meteorological Society, 98*(3), 449-459. doi:10.1175/bams-d-15-00245.1
585 DeFlorio, M. J., Waliser, D. E., Guan, B., Lavers, D. A., Ralph, F. M., & Vitart, F. (2018). Global
586 Assessment of Atmospheric River Prediction Skill. *Journal of Hydrometeorology, 19*(2),
587 409-426. doi:10.1175/Jhm-D-17-0135.1
588 DeFlorio, M. J., Waliser, D. E., Guan, B., Ralph, F. M., & Vitart, F. (2018). Global evaluation of
589 atmospheric river subseasonal prediction skill. *Climate Dynamics, 52*(5-6), 3039-3060.
590 doi:10.1007/s00382-018-4309-x
591 Dettinger, M. D. (2013). Atmospheric Rivers as Drought Busters on the US West Coast. *Journal*
592 *of Hydrometeorology, 14*(6), 1721-1732. doi:10.1175/Jhm-D-13-02.1
593 Dettinger, M. D., Ralph, F. M., Das, T., Neiman, P. J., & Cayan, D. R. (2011). Atmospheric Rivers,
594 Floods and the Water Resources of California. *Water, 3*(2), 445-478.
595 doi:10.3390/w3020445
596 Eichler, T., & Higgins, W. (2006). Climatology and ENSO-Related Variability of North American
597 Extratropical Cyclone Activity. *Journal of Climate, 19*(10), 2076-2093.
598 doi:10.1175/JCLI3725.1
599 Espinoza, V., Waliser, D. E., Guan, B., Lavers, D. A., & Ralph, F. M. (2018). Global Analysis of
600 Climate Change Projection Effects on Atmospheric Rivers. *Geophysical Research Letters,*
601 *45*(9), 4299-4308. doi:10.1029/2017gl076968
602 Gelaro, R., McCarty, W., Suarez, M. J., Todling, R., Molod, A., Takacs, L., . . . Zhao, B. (2017).
603 The Modern-Era Retrospective Analysis for Research and Applications, Version 2
604 (MERRA-2). *J Clim, Volume 30*(Iss 13), 5419-5454. doi:10.1175/JCLI-D-16-0758.1

Gershunov, A., & Barnett, T. P. (1998). ENSO Influence on Intraseasonal Extreme Rainfall and Temperature Frequencies in the Contiguous United States: Observations and Model Results. *Journal of Climate, 11*(7), 1575-1586. doi:10.1175/1520-0442(1998)011<1575:Eioier>2.0.Co;2

Gershunov, A., Shulgina, T., Ralph, F. M., Lavers, D. A., & Rutz, J. J. (2017). Assessing the climate-scale variability of atmospheric rivers affecting western North America. *Geophysical Research Letters, 44*(15), 7900-7908. doi:10.1002/2017gl074175

Gill, A. E. (1980). Some simple solutions for heat-induced tropical circulation. *Quarterly Journal of the Royal Meteorological Society, 106*(449), 447-462. doi:10.1002/qj.49710644905

Gorodetskaya, I. V., Tsukernik, M., Claes, K., Ralph, M. F., Neff, W. D., & Van Lipzig, N. P. M. (2014). The role of atmospheric rivers in anomalous snow accumulation in East Antarctica. *Geophysical Research Letters, 41*(17), 6199-6206. doi:10.1002/2014gl060881

Guan, B., Molotch, N. P., Waliser, D. E., Fetzer, E. J., & Neiman, P. J. (2013). The 2010/2011 snow season in California's Sierra Nevada: Role of atmospheric rivers and modes of large-scale variability. *Water Resources Research, 49*(10), 6731-6743. doi:10.1002/wrcr.20537

Guan, B., & Waliser, D. E. (2015). Detection of atmospheric rivers: Evaluation and application of an algorithm for global studies. *Journal of Geophysical Research-Atmospheres, 120*(24), 12514-12535. doi:10.1002/2015jd024257

Guan, B., Waliser, D. E., Molotch, N. P., Fetzer, E. J., & Neiman, P. J. (2012). Does the Madden–Julian Oscillation Influence Wintertime Atmospheric Rivers and Snowpack in the Sierra Nevada? *Monthly Weather Review, 140*(2), 325-342. doi:10.1175/mwr-d-11-00087.1

626 Halpern, D., & Woiceshyn, P. M. (1999). Onset of the Somali Jet in the Arabian Sea during June
627 1997. *Journal of Geophysical Research: Oceans, 104*(C8), 18041-18046.
628 doi:10.1029/1999jc900141
629 Hirsch, M. E., DeGaetano, A. T., & Colucci, S. J. (2001). An East Coast Winter Storm Climatology.
630 *Journal of Climate, 14*(5), 882-899. doi:10.1175/1520-
631 0442(2001)014<0882:Aecwsc>2.0.Co;2
632 Hoerling, M. P., Kumar, A., & Zhong, M. (1997). El Niño, La Niña, and the Nonlinearity of Their
633 Teleconnections. *Journal of Climate, 10*(8), 1769-1786. doi:10.1175/1520-
634 0442(1997)010<1769:Enolna>2.0.Co;2
635 Holloway, C. E., & Neelin, J. D. (2009). Moisture Vertical Structure, Column Water Vapor, and
636 Tropical Deep Convection. *Journal of the Atmospheric Sciences, 66*(6), 1665-1683.
637 doi:10.1175/2008jas2806.1
638 Hu, H., Dominguez, F., Wang, Z., Lavers, D. A., Zhang, G., & Ralph, F. M. (2017). Linking
639 Atmospheric River Hydrological Impacts on the U.S. West Coast to Rossby Wave
640 Breaking. *Journal of Climate, 30*(9), 3381-3399. doi:10.1175/jcli-d-16-0386.1
641 Huang, B., Thorne, P. W., Banzon, V. F., Boyer, T., Chepurin, G., Lawrimore, J. H., . . . Zhang,
642 H. (2017). Extended Reconstructed Sea Surface Temperature, Version 5 (ERSSTv5):
643 Upgrades, Validations, and Intercomparisons. *Journal of Climate, 30*(20), 8179-8205.
644 doi:10.1175/jcli-d-16-0836.1
645 Huning, L. S., Margulis, S. A., Guan, B., Waliser, D. E., & Neiman, P. J. (2017). Implications of
646 Detection Methods on Characterizing Atmospheric River Contribution to Seasonal
647 Snowfall Across Sierra Nevada, USA. *Geophysical Research Letters, 44*(20), 10,445-
648 410,453. doi:10.1002/2017gl075201

649 Kim, H., Zhou, Y., & Alexander, M. A. (2017). Changes in atmospheric rivers and moisture
650 transport over the Northeast Pacific and western North America in response to ENSO
651 diversity. *Climate Dynamics*, 1-14. doi:10.1007/s00382-017-3598-9
652 Lau, K. M., & Chan, P. H. (1988). Intraseasonal and Interannual Variations of Tropical Convection:
653 A Possible Link between the 40–50 Day Oscillation and ENSO? *Journal of the*
654 *Atmospheric Sciences, 45*(3), 506-521. doi:10.1175/1520-
655 0469(1988)045<0506:Iaivot>2.0.Co;2
656 Lavers, D. A., Allan, R. P., Villarini, G., Lloyd-Hughes, B., Brayshaw, D. J., & Wade, A. J. (2013).
657 Future changes in atmospheric rivers and their implications for winter flooding in Britain.
658 *Environmental Research Letters, 8*(3). doi:Artn 03401010.1088/1748-9326/8/3/034010
659 Lavers, D. A., Allan, R. P., Wood, E. F., Villarini, G., Brayshaw, D. J., & Wade, A. J. (2011).
660 Winter floods in Britain are connected to atmospheric rivers. *Geophysical Research Letters*,
661 *38*(23), L23803. doi:Artn L2380310.1029/2011gl049783
662 Lavers, D. A., Pappenberger, F., & Zsoter, E. (2014). Extending medium-range predictability of
663 extreme hydrological events in Europe. *Nature Communications, 5*, 5382.
664 doi:10.1038/ncomms6382
665 Liebmann, B., & Smith, C. A. (1996). Description of a complete (interpolated) outgoing longwave
666 radiation dataset. *Bulletin of the American Meteorological Society, 77*(6), 1275-1277.
667 Retrieved from <Go to ISI>://WOS:A1996VC04300013
668 Lora, J. M., Mitchell, J. L., Risi, C., & Tripati, A. E. (2017). North Pacific atmospheric rivers and
669 their influence on western North America at the Last Glacial Maximum. *Geophysical*
670 *Research Letters, 44*(2), 1051-1059. doi:10.1002/2016gl071541

671 Maloney, E. D., & Hartmann, D. L. (2000). Modulation of Hurricane Activity in the Gulf of
672 Mexico by the Madden-Julian Oscillation. *Science, 287*(5460), 2002.
673 doi:10.1126/science.287.5460.2002
674 McClenny, E., Ullrich, P. A., Grotjahn, R. (2020) Sensitivity of atmospheric river vapor transport
675 and precipitation to uniform sea-surface temperature increases.
676 https://doi.org/10.5281/zenodo.3659310
677 McGuirk, J. P., Thompson, A. H., & Smith, N. R. (1987). Moisture Bursts over the Tropical Pacific
678 Ocean. *Monthly Weather Review, 115*(4), 787-798. doi:10.1175/1520-
679 0493(1987)115<0787:Mbottp>2.0.Co;2
680 Mo, K. C. (2000). The Association between Intraseasonal Oscillations and Tropical Storms in the
681 Atlantic Basin. *Monthly Weather Review, 128*(12), 4097-4107. doi:10.1175/1520-
682 0493(2000)129<4097:Tabioa>2.0.Co;2
683 Moon, J. Y., Wang, B., & Ha, K. J. (2011). ENSO regulation of MJO teleconnection. *Climate*
684 *Dynamics, 37*(5-6), 1133-1149. doi:10.1007/s00382-010-0902-3
685 Mundhenk, B. D., Barnes, E. A., & Maloney, E. D. (2016). All-Season Climatology and
686 Variability of Atmospheric River Frequencies over the North Pacific. *Journal of Climate,*
687 *29*(13), 4885-4903. doi:10.1175/Jcli-D-15-0655.1
688 Mundhenk, B. D., Barnes, E. A., Maloney, E. D., & Baggett, C. F. (2018). Skillful empirical
689 subseasonal prediction of landfalling atmospheric river activity using the Madden–Julian
690 oscillation and quasi-biennial oscillation. *npj Climate and Atmospheric Science*, *1*(1),
691 20177. doi:10.1038/s41612-017-0008-2
692 Neiman, P. J., Ralph, F. M., Moore, B. J., Hughes, M., Mahoney, K. M., Cordeira, J. M., &
693 Dettinger, M. D. (2013). The Landfall and Inland Penetration of a Flood-Producing

694 Atmospheric River in Arizona. Part I: Observed Synoptic-Scale, Orographic, and
695 Hydrometeorological Characteristics. *Journal of Hydrometeorology, 14*(2), 460-484.
696 doi:10.1175/Jhm-D-12-0101.1
697 Neiman, P. J., Ralph, F. M., Wick, G. A., Lundquist, J. D., & Dettinger, M. D. (2008).
698 Meteorological characteristics and overland precipitation impacts of atmospheric rivers
699 affecting the West Coast of North America based on eight years of SSM/I satellite
700 observations. *Journal of Hydrometeorology, 9*(1), 22-47. doi:10.1175/2007jhm855.1
701 Newell, R. E., Newell, N. E., Zhu, Y., & Scott, C. (1992). Tropospheric Rivers - a Pilot-Study.
702 *Geophysical Research Letters, 19*(24), 2401-2404. doi:Doi 10.1029/92gl02916
703 O'Brien, T. A., Risser, M. D., Loring, B., Elbashandy, A. A., Krishnan, H., Johnson, J., . . . Collins,
704 W. D. (2020). Detection of Atmospheric Rivers with Inline Uncertainty Quantification:
705 TECA-BARD v1.0. *Geosci. Model Dev. Discuss., 2020*, 1-20. doi:10.5194/gmd-2020-55
706 Patricola, C. M., O'Brien, J. P., Risser, M. D., Rhoades, A. M., O'Brien, T. A., Ullrich, P. A., . . .
707 Collins, W. D. (2020). Maximizing ENSO as a source of western US hydroclimate
708 predictability. *Climate Dynamics, 54*(1-2), 351-372. doi:10.1007/s00382-019-05004-8
709 Payne, A. E., & Magnusdottir, G. (2014). Dynamics of Landfalling Atmospheric Rivers over the
710 North Pacific in 30 Years of MERRA Reanalysis. *Journal of Climate, 27*(18), 7133-7150.
711 doi:10.1175/Jcli-D-14-00034.1
712 Payne, A. E., & Magnusdottir, G. (2015). An evaluation of atmospheric rivers over the North
713 Pacific in CMIP5 and their response to warming under RCP 8.5. *Journal of Geophysical*
714 *Research-Atmospheres, 120*(21), 11173-11190. doi:10.1002/2015jd023586
715 Radic, V., Cannon, A. J., Menounos, B., & Gi, N. (2015). Future changes in autumn atmospheric
716 river events in British Columbia, Canada, as projected by CMIP5 global climate models.

Journal of Geophysical Research-Atmospheres, 120(18), 9279-9302. doi:10.1002/2015jd023279

Ralph, F. M., Neiman, P. J., Kiladis, G. N., Weickmann, K., & Reynolds, D. W. (2011). A Multiscale Observational Case Study of a Pacific Atmospheric River Exhibiting Tropical-Extratropical Connections and a Mesoscale Frontal Wave. *Monthly Weather Review, 139*(4), 1169-1189. doi:10.1175/2010mwr3596.1

Ralph, F. M., Neiman, P. J., Wick, G. A., Gutman, S. I., Dettinger, M. D., Cayan, D. R., & White, A. B. (2006). Flooding on California's Russian River: Role of atmospheric rivers. *Geophysical Research Letters, 33*(13). doi:Artn L1380110.1029/2006gl026689

Ralph, F. M., Rutz, J. J., Cordeira, J. M., Dettinger, M., Anderson, M., Reynolds, D., . . . Smallcomb, C. (2019). A Scale to Characterize the Strength and Impacts of Atmospheric Rivers. *Bulletin of the American Meteorological Society, 100*(2), 269-290. doi:10.1175/Bams-D-18-0023.1

Ralph, F. M., Wilson, A. M., Shulgina, T., Kawzenuk, B., Sellars, S., Rutz, J. J., . . . Wick, G. A. (2018). ARTMIP-early start comparison of atmospheric river detection tools: how many atmospheric rivers hit northern California's Russian River watershed? *Climate Dynamics, 52*(7-8), 4973-4994. doi:10.1007/s00382-018-4427-5

Rhoades, A. M., Jones, A. D., O'Brien, T. A., O'Brien, J. P., Ullrich, P. A., & Zarzycki, C. M. (2020). Influences of North Pacific Ocean Domain Extent on the Western U.S. Winter Hydroclimatology in Variable-Resolution CESM. *Journal of Geophysical Research: Atmospheres, 125*(14), e2019JD031977. doi:10.1029/2019jd031977

Rutz, J. J., Shields, C. A., Lora, J. M., Payne, A. E., Guan, B., Ullrich, P., . . . Viale, M. (2019). The Atmospheric River Tracking Method Intercomparison Project (ARTMIP):

Quantifying Uncertainties in Atmospheric River Climatology. *Journal of Geophysical Research: Atmospheres, 124*(24), 13777-13802. doi:10.1029/2019jd030936

Rutz, J. J., Steenburgh, W. J., & Ralph, F. M. (2014). Climatological Characteristics of Atmospheric Rivers and Their Inland Penetration over the Western United States. *Monthly Weather Review, 142*(2), 905-921. doi:10.1175/Mwr-D-13-00168.1

Ryoo, J. M., Kaspi, Y., Waugh, D. W., Kiladis, G. N., Waliser, D. E., Fetzer, E. J., & Kim, J. (2013). Impact of Rossby Wave Breaking on U.S. West Coast Winter Precipitation during ENSO Events. *Journal of Climate, 26*(17), 6360-6382. doi:10.1175/Jcli-D-12-00297.1

Sellars, S. L., Gao, X. G., & Sorooshian, S. (2015). An Object-Oriented Approach to Investigate Impacts of Climate Oscillations on Precipitation: A Western United States Case Study. *Journal of Hydrometeorology, 16*(2), 830-842. doi:10.1175/Jhm-D-14-0101.1

Sellars, S. L., Nguyen, P., Chu, W., Gao, X., Hsu, K. L., & Sorooshian, S. (2013). Computational Earth Science: Big Data Transformed Into Insight. *Eos, Transactions American Geophysical Union, 94*(32), 277-278. doi:10.1002/2013eo320001

Shearer, E. J., Nguyen, P., Sellars, S. L., Analui, B., Kawzenuk, B., Hsu, K. L., & Sorooshian, S. (2020). The Atmospheric River-CONNected objeECT (AR-CONNECT) algorithm applied to the National Aeronautics and Space Administration (NASA) Modern-Era Retrospective Analysis for Research and Applications, Version 2 (MERRA V2) - 1983 to 2016. UC San Diego Library Digital Collections. https://doi.org/10.6075/J0D21W00

Shields, C. A., & Kiehl, J. T. (2016a). Atmospheric river landfall-latitude changes in future climate simulations. *Geophysical Research Letters, 43*(16), 8775-8782. doi:10.1002/2016gl070470

762 Shields, C. A., & Kiehl, J. T. (2016b). Simulating the Pineapple Express in the half degree
763 Community Climate System Model, CCSM4. *Geophysical Research Letters, 43*(14), 7767-
764 7773. doi:10.1002/2016gl069476
765 Shields, C. A., Rutz, J. J., Leung, L. Y., Ralph, F. M., Wehner, M., Kawzenuk, B., . . . Nguyen, P.
766 (2018). Atmospheric River Tracking Method Intercomparison Project (ARTMIP): project
767 goals and experimental design. *Geoscientific Model Development, 11*(6), 2455-2474.
768 doi:10.5194/gmd-11-2455-2018
769 Spry, C. M., Kohfeld, K. E., Allen, D. M., Dunkley, D., & Lertzman, K. (2014). Characterizing
770 Pineapple Express storms in the Lower Mainland of British Columbia, Canada. *Canadian*
771 *Water Resources Journal, 39*(3), 302-323. doi:10.1080/07011784.2014.942574
772 Stan, C., Straus, D. M., Frederiksen, J. S., Lin, H., Maloney, E. D., & Schumacher, C. (2017).
773 Review of Tropical-Extratropical Teleconnections on Intraseasonal Time Scales. *Reviews*
774 *of Geophysics, 55*(4), 902-937. doi:10.1002/2016rg000538
775 Waliser, D. E., & Guan, B. (2017). Extreme winds and precipitation during landfall of atmospheric
776 rivers. *Nature Geoscience, 10*(3), 179-U183. doi:10.1038/Ngeo2894
777 Wheeler, M. C., & Hendon, H. H. (2004). An all-season real-time multivariate MJO index:
778 Development of an index for monitoring and prediction. *Monthly Weather Review, 132*(8),
779 1917-1932. doi:Doi 10.1175/1520-0493(2004)132<1917:Aarmmi>2.0.Co;2
780 Williams, I. N., & Patricola, C. M. (2018). Diversity of ENSO Events Unified by Convective
781 Threshold Sea Surface Temperature: A Nonlinear ENSO Index. *Geophysical Research*
782 *Letters, 45*(17), 9236-9244. doi:10.1029/2018gl079203

783 Zhou, Y., & Kim, H. (2017). Prediction of atmospheric rivers over the North Pacific and its
784 connection to ENSO in the North American multi-model ensemble (NMME). *Climate*
785 *Dynamics*. doi:10.1007/s00382-017-3973-6
786 Zhou, Y., & Kim, H. (2019). Impact of Distinct Origin Locations on the Life Cycles of Landfalling
787 Atmospheric Rivers Over the U.S. West Coast. *Journal of Geophysical Research:*
788 *Atmospheres, 124*(22), 11897-11909. doi:10.1029/2019jd031218
789 Zhou, Y., Kim, H., & Guan, B. (2018). Life Cycle of Atmospheric Rivers: Identification and
790 Climatological Characteristics. *Journal of Geophysical Research-Atmospheres, 123*(22),
791 12715-12725. doi:10.1029/2018jd029180
792 Zhu, Y., & Newell, R. E. (1994). Atmospheric Rivers and Bombs. *Geophysical Research Letters,*
793 *21*(18), 1999-2002. doi:10.1029/94gl01710
794
795